Poor performance of a common crevasse model at marine-terminating glaciers

Ellyn M. Enderlin[1], Timothy C. Bartholomaus[2]

[1]Department of Geosciences, Boise State University, Boise, Idaho, 83725, USA

5 [2]Department of Geological Sciences, University of Idaho, Moscow, Idaho, 83844, USA

Correspondence to: Ellyn M. Enderlin (ellynenderlin@boisestate.edu)

Abstract. Crevasses are both affected by and effect stresses and surface mass balance of glaciers, potentially exerting important controls on meltwater routing, glacier viscosity, and iceberg calving, yet there are few direct observations of crevasse depth. Here we assess one of the most common models for crevasse formation, in which crevasse depths depend on the local stress

10 state, through analysis of 52644 crevasse depth observations from 19 Greenland glaciers. We find that modeled depths are uncorrelated with observed depths and are generally too deep. Model performance can be improved with glacier-by-glacier tuning of viscosity and water depth parameters, but spatial variations in tuning parameters are unlikely to have a physical basis, and the model still fails to capture smaller-scale variations in crevassing that may control calving. Thus, numerical ice flow models drawing on this parameterization are likely to yield inaccurate projections of glacier mass change or crevasse depth-

15 driven terminus position changes.

1 Introduction

The geometry and concentration of crevasses are both affected by and effect the stress state and surface mass balance of glaciers, ice shelves, and ice sheets (Colgan et al., 2016). Changes in crevasse geometry and concentration can arise as the result of long-term or rapid changes in stress state, serving as a valuable tool to infer the onset of kinematic change (Colgan et

20 al., 2011; Trantow and Herzfeld, 2018). These changes can also influence the stress state. For example, changes in crevassing within lateral shear margins of Antarctic ice streams have the potential to dramatically alter the ability of ice streams to buttress flow from the interior, in turn exerting an important control on ice sheet stability (Borstad et al., 2016; Reese et al., 2018). The impoundment of surface meltwater runoff in crevasses can promote crevasse penetration and assist in the penetration of meltwater to the glacier bed (van der Veen, 1998; Stevens et al., 2015; Poinar et al., 2017), influencing the englacial and basal

25 stress states. Crevasses also increase surface roughness, altering the incidence angle of solar radiation and turbulent energy fluxes, which in turn influence surface melt production (Pfeffer and Bretherton, 1987; Andreas, 2002; Hock, 2005; Cathles et al., 2011; Colgan et al., 2016).

These interactions between crevasses, stresses, and surface mass balance make crevasses particularly important components

30 of terrestrial ice, particularly near the termini of the marine-terminating glaciers and ice streams draining Greenland and Antarctica. In Antarctica, observations and models indicate that the ice shelves fringing the continent are highly vulnerable to

widespread crevasse hydrofracture in a warming climate (Pollard et al., 2015; Rott et al., 1996; Scambos et al., 2000, 2009). The influence of crevasses, and changes in crevassing over time due to atmospheric warming, are less clear for Arctic marine-terminating glaciers. Despite the abundance of crevasses throughout the marginal zone of the Greenland ice sheet, there are
35   few observations of crevasse depths at Greenland's glaciers. However, the coincident increase in surface meltwater runoff and widespread retreat of glacier termini across Greenland (Carr et al., 2017; Howat and Eddy, 2011; Moon and Joughin, 2008) suggests that hydrofracture may exert a first-order control on calving (Benn et al., 2007a).

Since calving involves the mechanical detachment of ice from a glacier terminus, it has been assumed that calving occurs when
40   and where surface crevasses penetrate the full ice thickness (Benn et al., 2007a). For closely-spaced crevasses, concentration of stresses at crevasse tips can be ignored and surface crevasse depths can be estimated using the Nye formulation (Nye, 1957), such that

$$d_{modeled} = \frac{2}{\rho_i g}\left(\frac{\dot{\varepsilon}_{xx} - \dot{\varepsilon}_{crit}}{A}\right)^{1/3} + \frac{\rho_w}{\rho_i} h_w \ , \tag{1}$$

where ρ_i and ρ_w are the densities of ice (917 kg m^{-3}) and water (1000 kg m^{-3}), g is gravitational acceleration (9.81 m s^{-2}), $\dot{\varepsilon}_{xx}$
45   is the longitudinal strain rate (yr^{-1}), $\dot{\varepsilon}_{crit}$ is the critical strain rate threshold for crevasse formation (yr^{-1}), A is the creep parameter describing ice viscosity (Pa^{-3} yr^{-1}), and h_w is the depth of water in crevasses. Using this formulation, crevasse deepening can be driven by either increased surface meltwater impoundment or enhanced longitudinal stretching.

When implemented in numerical ice flow models as the terminus boundary condition, an open connection between the ocean
50   and crevasses penetrating to sea level is assumed, which allows abundant water to drive full-thickness crevasse propagation, i.e., calving; the terminus is shifted accordingly (Benn et al., 2007b). This crevasse depth parameterization has been used to simulate terminus position change for several large glaciers around the Greenland periphery (Cook et al., 2014; Nick et al., 2013; Vieli and Nick, 2011). However, crevasse depth observations from Breiðamerkurjökull, Iceland, suggest that the Nye formulation may over-estimate crevasse depths by a factor of two (Mottram and Benn, 2009). Despite the over-estimation, it
55   remains assumed that, at the least, crevasse depths are related to local stresses. Failure of the Nye formulation, as well as more complex models for crevasse formation and propagation, are attributed to inaccuracies in other underlying assumptions and parameterizations of the models rather than the dependence on local stresses (Benn et al., 2007a; van der Veen, 1998). While ice viscosity or water depth in crevasses can conceivably be tuned in Eq. (1) to match observations, there is no assurance that the model accounts for the primary control(s) on terminus change. Furthermore, the high sensitivity of simulated terminus
60   positions to relatively small (~1-10 m) changes in water depth (Cook et al., 2012, 2014; Otero et al., 2017) lead us to question the appropriateness of this model. Because model projections of dynamic mass loss may well be in error if driven by an inaccurate calving law, increased confidence in dynamic mass loss projections drawing on this calving law requires validation of modeled crevasse depths.

Here we construct the first extensive record of crevasse depths for Greenland's fast-flowing outlet glaciers using airborne lidar and high-resolution digital elevation models from 2011-2018. We apply these observed crevasse depths and modeled crevasse depths from satellite-derived strain rates to assess the accuracy of modeled crevasse depths. Furthermore, we examine the likelihood that spatio-temporal variations in crevasse depth can explain observed variations in terminus position change and associated dynamic mass loss for Greenland's marine-terminating outlet glaciers. Although we focus on Greenland, our assessment of 19 glaciers spanning a wide range of geometries, climate regimes, and dynamic histories (Fig. 1a) ensures that the results of our analysis are broadly applicable to glaciers throughout the Arctic.

2 Methods

2.1 Observed Crevasse Depths

We construct time series of crevasse depths from flow-following lidar swaths acquired by NASA Operation IceBridge (OIB) and 2 m-resolution digital elevation models (DEMs) using a semi-automated approach that identifies crevasses from local elevation minima (Figs. 1b-e). We use lidar observations from the OIB ATM (Advanced Topographic Mapper), which has a vertical precision of better than 1cm and spatial sampling of one pulse every ~10 m^2 within its conical swath (https://nsidc.org/data/ilatm1b). Repeat April/May flow-following observations are available for all our study sites during the 2013-2018 period. Elevations were also extracted from 2 m-resolution DEMs produced by the Polar Geospatial Center as part of the ArcticDEM program. The WorldView DEMs are less precise (3m vertical uncertainty (Noh and Howat, 2015)) but provided estimates of elevation throughout the 2011-2018 melt seasons. We used an average of ~4 lidar swaths and ~16 DEMs per glacier for our analysis.

Lidar swaths were overlain on cloud-free summer Landsat 8 images and swath centerlines were manually traced to the inland extents of visible crevassing. Using a moving window approach, shifted at ~1 m increments along the swath centerlines, we linearly interpolated the nearest elevation data, then identified crevasses using a filtering process described below and illustrated for Kong Oscar Gletsjer in Fig. 1. To identify crevasses, centerline elevations were first detrended over the ~500 m-wide moving window (Fig. 1b inset), then the local elevation minimum and maximum from were extracted from each of three smaller windows centered on the detrended profile (Fig. 1b, gray shading). The process was repeated over the full profile length, resulting in the identification of local lows and highs for each elevation profile. The minimum (maximum) elevation was identified from each grouping of contiguous low (high) points and the remaining points were discarded (Fig. 1c). For each minimum, the closest neighboring down- and up-glacier maxima were used to define longitudinal crevasse extent (Fig. 1d). Potential collapsed seracs at the bottom of crevasses and small surface irregularities less than the vertical uncertainty of the DEMs were discarded.

The appropriate lengths for the detrending window and search windows to identify the local minima were determined through a comparison of manual and automated crevasse depth distributions (i.e., depths and their locations) from the most complete lidar profile for each glacier. Six detrending window sizes and two sets of search window sizes were tested, for a total of 12 test combinations, as outlined in Table S1. The range of possible detrending window sizes was constrained by the requirements

100   that the window (1) spanned the largest crevasses (~200 m in width at Helheim Glacier) and (2) did not exceed the maximum half-wavelength of large-scale oscillations in surface elevation evident along the profiles (~800-1500m). The tested search window sizes minimally spanned the maximum observed half-width of crevasses, but fully spanned the majority of crevasses: the median width (± median of the absolute value of deviation (MAD)) of the 3264 manually-identified crevasses was 19.2m ± 6.9m and the maximum width was 183.9m. The optimal window combination used for automated crevasse identification

105   was the window combination that yielded the smallest number of falsely-identified crevasses (both false positives and false negatives) and the smallest depth misfit relative to the manually-extracted dataset. Optimal window sizes were glacier-dependent. The optimal detrending window sizes ranged from 350-800m (9=350m, 2=500, 3=550, 1=650, 4=800). The smaller search window sizes were considered optimal for all study sites except Helheim Glacier, which had the widest crevasses.

110   Although V-shaped crevasses were common at all study sites, more complex geometries were also prevalent. Based on the commonality of V-shaped crevasses, we assumed that crevasses initially formed with V shapes, and that apparent deviations from a V-shaped geometry were due to serac toppling, over-printing of new crevasses on previously damaged ice (Colgan et al., 2016), or the presence of impounded meltwater. To better represent the depth of fractured ice, we linearly projected crevasse walls to depth and identified their extrapolated point of intersection (Fig. 1e). For each elevation minimum and closest neighboring down- and up-glacier maxima, the crevasse walls were identified as contiguous regions with slopes within the

115   typical range observed for manually-identified V-shaped crevasses in the window-calibration elevation profiles. Since there is no physical reason why the crevasse wall surface slopes should be normally distributed, we used the median ± 1.4826 MAD to characterize the typical range. For normally distributed data, this formulation would be analogous to the mean ± standard deviation. For irregularly-shaped crevasses and for crevasses located where the rough glacier surface resulted in local elevation

120   maxima several meters to tens of meters from the crevasse edge, this approach retracted the crevasse wall extents to correspond with slope breaks. If wall slopes were entirely outside of the typical range, there was no effect on the crevasse extents. Average crevasse wall surface slopes were used to project crevasses to depth. We refer to the average elevation difference between the top and bottom of crevasses as the observed crevasse depths.

125   We estimated uncertainties associated with (1) spatial resolution of the remotely-sensed datasets through comparisons of same-day profiles, (2) the automated approach for crevasse identification through comparisons with depths from manually-identified crevasses, and (3) crevasse depth extrapolation through comparisons between observed and extrapolated depths for V-shaped crevasses. All values presented are the median +/- the median of the absolute value of deviation from the median (i.e., MAD) unless otherwise stated.

130

Although the precision of the lidar elevations is better than 1cm, the discrete sampling of the lidar may not be coincident with the location of the true crevasse bottom. Uncertainties associated with the lidar spatial sampling were quantified through a comparison of crevasse depths extracted from same-day up- and down-glacier swaths. The difference in crevasse depths between repeat swaths was -0.35±1.7 m. We attribute the non-zero mean depth difference to potential mismatches in the depth

135 comparison: depths for nearest neighboring crevasses were used in our calculation but advection between swaths introduces some ambiguity where speeds were fast and crevasses were densely packed. Uncertainties associated with the inclusion of the lower resolution WorldView DEM-derived depths were estimated through a comparison of same day lidar- and DEM-derived crevasse depths. We found that the DEM-derived depths were 0.99m less than the lidar-derived depths, with a MAD of 2.5 m. A comparison of high-resolution and 2m-resolution lidar-derived crevasse depths indicated the decrease in horizontal

140 resolution of the DEMs accounted for ~1/3 of the DEM-derived depth bias. Since the potential biases were within the uncertainties in the datasets, we do not discuss them further. The lidar-derived depth uncertainty and the MAD from the lidar-DEM depth comparison were summed in quadrature to obtain a DEM-derived depth uncertainty of 3.0 m.

Uncertainties associated with automated crevasse depth estimation were quantified through a comparison of manually- and

145 automatically-extracted crevasse depths. Automation uncertainties were minimized through the use of manual calibration datasets. Typical uncertainties introduced by the use of our automated approach were -0.3±0.4 m, indicating that the automated approach slightly over-estimated crevasse depths due to differences in the manual versus automated identification of crevasse wall limits.

150 Our assumption of V-shaped crevasses was supported by observations of abundant V-shaped crevasses in every elevation profile examined here. For the V-shaped crevasses identified in the calibration profiles, the difference between the observed and extrapolated depths was <0.1m on average. Examples of V-shaped crevasses can be found in Fig. 1 and scatterplots comparing observed and extrapolated depths for V-shaped and irregularly-shaped crevasses are shown in Fig. S1.

155 Overall, we estimate a lidar-derived and DEM-derived depth uncertainties of 1.7 m and 3.0 m, respectively, with the tendency toward slight under-estimation of crevasse depths (1.0 m bias) when using DEMs. Automation results in a slight over-estimation (0.3 m) of crevasse depths due to differences in the manual and automated crevasse wall extents. The difference between observed and extrapolated crevasse depths for V-shaped crevasses is <0.1 m, indicating an excellent linear crevasse wall approximation and inconsequential bias associated with extrapolated depths (Fig. S1).

160

2.2 Modeled Crevasse Depths

Modeled crevasse depths were calculated using the Nye formulation for densely-spaced crevasses such that crevasses penetrate to the depth that local longitudinal stresses are balanced by the lithostatic stress induced by the weight of the overlying ice column (Eqn. 1). Using this formulation, crevasses are only found under tension, with the deepest crevasses in locations with

165   high longitudinal strain rates and more viscous (i.e., colder and/or less damaged) ice. The Nye formulation does not account for any 'inheritance', meaning the crevasse depths are estimated as a function of the local, instantaneous, longitudinal strain rate without consideration of crevasse advection.

Strain rates were computed from NASA Making Earth System Data Records for Use in Research Environments (MEaSUREs)

170   Interferometric Synthetic Aperture Radar velocities (https://nsidc.org/data/NSIDC-0481/versions/1). The temporal coverage of these approximately bi-weekly velocity fields varied widely between glaciers, with an average of 66 velocity maps per glacier and a maximum of 282 maps for Jakobshavn from 2011-2018. Spatial gradients in velocity were used to compute strain rates in the native (polar stereographic) coordinate system, which were then rotated into flow-following coordinates and linearly interpolated to the swath centerlines. Modeled crevasse depths were calculated from the longitudinal strain rate profiles

175   using Eq. (1).

The creep parameter (A) is dependent on a number of variables, including ice temperature, crystal fabric development, and damage, but is poorly constrained by observations. Here, we approximated temperature-dependent spatial variations in the creep parameter as a linear function of latitude so that they were in agreement with values in the crevasse penetration depth-

180   forced prognostic ice flow model simulations of Nick et al. (2013).

For our initial estimates, what we term the 'minimal' model, we followed the approach of Mottram and Benn (2009) and assumed crevasses formed everywhere under tension (i.e., no critical strain rate threshold) and there was no water in crevasses (likely for the case of spring OIB data). To improve model performance, we also tested several more complex versions of the

185   model. We first estimated the critical strain rate for crevasse formation at each glacier as the maximum strain rate inland of the most up-glacier crevasse observation. To quantify the effects of potential spatial variations in viscosity, we also used the crevasse observations to quantify a viscous deformation enhancement factor that effectively softens the ice and shallows predicted crevasses. Similar to Borstad et al. (2016), the deformation enhancement factor, D, was calculated from

$$d_{observed} = (1 - D) \left[\frac{2}{\rho_i g} \left(\frac{\dot{\varepsilon}_{xx}}{A} \right)^{1/3} \right]. \tag{2}$$

190   Substituting our initial modeled crevasse depths (i.e., Eq. (1) with $\dot{\varepsilon}_{crit} = 0$ and $h_w = 0$) in for the RHS term in brackets and rearranging to solve for the deformation enhancement factor, we obtained

$$D = \frac{d_{modeled} - d_{observed}}{d_{modeled}}. \tag{3}$$

The Cryosphere
Discussions

Although similar to damage in Borstad et al. (2016), our deformation enhancement factor is a function of spatial variations in damage, ice temperature, and crystal fabric. A unique deformation factor can be identified at each crevasse location using Eq.

195 (3). However, such detailed tuning is neither physically motivated nor practical for models, so we binned the data along-flow then parameterized deformation enhancement as a linear function of distance from the terminus using the binned data (Fig. S2). The deformation enhancement factors for the deepest crevasses in each 300 m bin were used in our parameterizations. Bin size did not influence along-flow patterns discussed below.

200 Finally, we used the inland-most deformation enhancement value to solve for modeled crevasse depths under the assumption of spatially uniform ice viscosity, then estimated impounded water depths from the misfit between the observed and modeled crevasse depths. Again, we sought a simple parameterization appropriate for use in numerical ice flow models: assuming that water depth varies with meltwater generation, we parameterized impounded water depth as linear function of surface elevation for each glacier (Fig. S3).

205

2.3 Crevasse Depth Comparison

To test the accuracy of modeled crevasse depths, we compared the maximum observed crevasse depths to median modeled crevasse depths computed using Equation 1. For this portion of the assessment, we use the simplest form of Equation 1, wherein there is no critical stress threshold for crevasse formation ($\dot{\varepsilon}_{crit} = 0$) and no water in crevasses ($h_w = 0$). We refer to this

210 version of the Nye formulation for crevasse depths as the minimal model hereafter. The comparison was performed over a wide range (50-2000 m) of spatial scales to account for variations in the spatial resolution of numerical models as well as potential variations in the distance over which stresses are transmitted.

3 Results

215 ### 3.1 Observed Crevasse Depths

We identified a total of 52644 crevasses in 381 elevation profiles among the 19 study glaciers. Broadly, crevasse occurrence increased towards each glacier terminus. Crevasse depth distributions are shown in Fig. 2 and depth profiles are shown in Fig. S4. We present statistics pertaining to crevasse depth and concentration, i.e., number of crevasses per kilometer, within 5 km of glacier termini in Table 1. Of all observed crevasses, the median depth was 6.2 m and median concentration was 17.2

220 crevasses per kilometer (one crevasse every 58 m). The crevasse concentrations span a fairly narrow range of values, with ~75% of crevasse concentrations between 15-19.7 crevasses km^{-1}, despite a wide range of glacier thicknesses and strain rates. The two relatively uncrevassed glaciers (concentrations less than 10 km^{-1}) have floating tongues and occur in the coldest, high latitude regions. The maximum observed depth of 64.9 m occurred at steep, fast-flowing Helheim Gletsjer. Helheim also had

225 the deepest median crevasse depth of 10.2 m. While some glaciers have more and deeper crevasses near the terminus than inland, this pattern is clearly not universal, and in many instances, crevasse depths decreased over the last several km of the terminus region (Figs. 2, S4).

Although the crevasse size distributions are dominated by a large number of relatively shallow (i.e., <10 m-deep) crevasses, we are primarily interested in the deepest crevasses, which are the most likely to penetrate the full glacier thickness and 230 therefore play an important role in large calving events and meltwater routing to the glacier bed. To isolate the deepest crevasses from the observations, we identified the maximum crevasse depth at 150 m-increments along flow so that the along-flow variations in crevasse depth had the same spatial resolution as the velocity data used to compute strain rates. To determine whether along-flow variations in maximum crevasse depth can be explained by either local variations in local longitudinal strain rates or strain history (i.e., longitudinal strain rate integrated along flow), we normalized the crevasse depth, strain rate, 235 and strain history data to facilitate direct comparison of their along-flow patterns. Data were normalized such that the minimum (maximum) observed value corresponds to a normalized value of zero (one). The normalized profiles in Fig. 3 suggest that along-flow variations in maximum crevasse depth cannot be simply explained as a function of variations in either local strain rate or strain history, although kilometer-scale variations in maximum crevasse depth at approximately half of the glaciers appear to follow patterns in strain history.

240

3.2 Crevasse Depth Comparison

At all spatial scales and over all time periods, the minimal model produced crevasse depths that were typically deeper than observed depths in extensional zones. However, the over-estimation of crevasse depths was not spatially consistent and the model failed to predict crevasses in compressional zones, as demonstrated for Inngia Isbræ in Fig. 4. Identical plots are 245 shown for the other glaciers in the supplemental material (Figs. S5-S22). In Fig. 4 and Figs. S5-S22, where modeled and observed crevasses were in good agreement, the data fall along the 1:1 line separating the white and gray regions. Where crevasses were observed but strain rates were negative, i.e., crevasse were missed by the model, the data fall along the x-axis. Although the maximum misfit and occurrence of missed crevasses decreased at longer spatial scales, discrepancies between observed and modeled depths on the order of tens of meters were observed at all spatial scales.

250

The comparisons of observed and modeled crevasse depths in Fig. 4 and Figs. S5-S22 also suggest that crevasse depths remained relatively stable at all study glaciers over the 2011-2018 period. Inngia Isbræ exhibited the largest dynamic change among our study glacier – the glacier retreated by ~4 km and thinned by ~100 m near the terminus (Fig. 4a) and flow accelerated by ~500 m/yr near the terminus (not shown) from 2012-2017 – yet nearly all observed crevasse depths remain < 255 30 m throughout the observation record (Fig. 4b). The highly-stacked appearance of the crevasse observations for all study glaciers in Fig. S4 also reflects the static nature of the kilometers-scale oscillations in crevasse depth visible for each glacier.

Uncertainties are not included in Fig. S4, but a large portion of the observed variations in crevasse depth are within the observational uncertainty of ~2-3 m for the observed depths.

260 We illustrate spatial variations in the discrepancy between modeled and observed crevasse depths at four study sites – Kong Oscar (northwest Greenland), Inngia (west), Daugaard-Jensen (east), and Heimdal (southeast) – in Fig. 5. For each panel, we represent temporal variability in modeled depths (driven by strain rate changes) in a minimal model (Fig. 5, orange shading, see Methods), but finding no clear pattern in the temporal variability, only identify modeled depths computed from the median speed profile for the remainder of our analysis (Fig. 5, colored lines). The complete set of plots, arranged geographically, are

265 included in the supplemental material (Fig. S23).

Additional model complexity, through tuning of the critical strain rate, viscosity, and impounded water depth parameters, provides inconsistent improvement of modeled crevasse depths. For example, one parameter with a clear physical motivation is the critical strain rate: because ice has tensile strength, crevasses will not exist where the strain rate does not exceed a tensile

270 strength threshold. We found that the addition of an observation-based non-zero critical strain rate value does not improve agreement between observed and modeled crevasse depths (Fig. 5; red lines). Instead, there is an increase in the extent of modeled no-crevasse regions without compensatory improvements in the accuracy of crevasse depths elsewhere. Discrepancies between the modeled and observed crevasses can also arise due to uncertainties in the parameterization of the viscosity of the ice. Profiles of a deformation enhancement factor that minimizes the misfit between observed and modeled

275 crevasse depths, shown in Fig. S2, suggest that the ice is considerably more ductile than predicted using a latitudinally-varying, temperature-dependent creep parameter: D generally exceeds 0.5, equivalent to an order of magnitude increase in the creep parameter. Inclusion of a deformation enhancement parameterization that varies linearly along flow results in improved model performance in extensional zones (Figs. 5, S23; green lines). However, in contrast with the expected along-flow increase in deformation enhancement due to strain heating, cryohydrologic warming, and mechanical damage, we find an along-flow

280 *decrease* in deformation enhancement for approximately half of the glaciers (Fig. S2).

The apparent decrease in deformation enhancement towards the termini is driven by an along-flow decrease in the misfit between observed and minimally-modeled crevasse depths. Assuming that crevasse water depths scale with meltwater runoff, then we would expect that the contribution of hydrofracture to observed depths should generally increase along-flow, potentially driving the decrease in the observed-modeled depth misfit. Using the inland-most deformation enhancement factor

285 and tuning impounded water depths to minimize the observed-modeled depth misfit, we obtain first-order estimates of modeled crevasse water depths. Water depths necessary for this minimization vary from ≤3.2 m for Zachariae Isstrøm to ≤32.7 m for Kong Oscar Gletsjer (Table 1). Modeled crevasse depths obtained using parameterized water depths are shown in Figs. 5 and S21 (blue lines). In line with expectations of increased water depth with enhanced surface meltwater runoff, we find that

290 approximately half of our glaciers displayed patterns of increasing water depth with decreasing surface elevation (Fig. S3).

However, the remaining half of glaciers showed either decreasing or no change in estimated water depths at the low-elevation, near-terminus regions. Inclusion of a simple parameterization that scales crevasse water depth as a linear function of elevation improved the model's ability to capture kilometers-scale patterns in crevasse depth (Fig. S23) but could not explain the smaller-scale oscillations in crevasse depth that we observed.

295

4 Discussion and Conclusions

Using the first spatially and temporally extensive record of surface crevasse depths for Greenland's fast-flowing marine-terminating glaciers, we find that there are typically >10 crevasses per kilometer but that the majority of crevasses are <10 m in depth. Given the skewed distributions of crevasse depths in Fig. 2, the inclusion of crevasses smaller than our detection
300   threshold of 3 m-depth would likely increase the concentration and decrease the median depths relative to those reported in Table 1. Crevasse depths are highly variable along flow, with pronounced changes in the shapes of the crevasse depth distributions and maximum crevasse depths evident at most glaciers (Figs. 2, 3). Although large-scale variations in maximum crevasse depth follow strain history at approximately half of our study sites (Fig. 3), small-scale patterns in crevasse depth cannot easily be explained by variations in local strain rate or strain history.

305

The disconnect between crevasse depths and local strain rates is emphasized by the failure of the Nye formulation to model crevasse depths. The spatially-variable discrepancy between modeled and observed crevasse depths is problematic because the crevasse depth calving parameterization uses the Nye formulation to prescribe the terminus position in numerical ice flow models. If calving is the result of crevasses penetrating to the waterline, then over-estimation of crevasse depths could result
310   in erroneous terminus retreat. The predicted absence of crevasses in compressional zones could also prevent modeled retreat, or lead to punctuated episodes of retreat and temporary stabilization, biasing projections of dynamic mass loss from marine-terminating glaciers.

Although there is undoubtedly some threshold stress below which crevasses will not form (see van der Veen (1998)), inclusion
315   of a non-zero threshold strain rate for crevasse formation does not improve model performance. We find that the modeled depths that incorporate deformation enhancement are generally in better agreement with observations than with the minimal model. This is not surprising since the deformation enhancement factor is calculated using the misfit between the modeled and observed crevasse depths. However, there is no clear physical explanation for the contrasting along-flow patterns in inferred enhancement, which suggest some glaciers have more viscous ice towards the terminus and others have less viscous (more
320   ductile) ice towards the terminus. The inferred water depths are even more problematic. There are few observations of hydrofracture in Greenland to which we can compare our inferred water depths but the spatial patterns are unrealistic – they can vary by tens of meters over hundreds of meters along flow and do not follow expected regional patterns in meltwater

runoff. Furthermore, approximately 1/4 of our observations were acquired prior to the onset of widespread seasonal surface melting, such that there should be no water impounded in crevasses. Therefore, even though model accuracy is improved by

325   tuning, the optimal deformation enhancement and water depth tuning parameters defined here have no physical basis and should not be used to improve model agreement with observations.

Based on the comparison of observed crevasse depths with local strain rates and strain history as well as the results of our tuning tests, we hypothesize that our inability to reproduce small-scale (i.e., sub-kilometer) variations in observed crevasse

330   depths using the Nye formulation stems from both its ignorance of advection and its assumption of reduced stress concentration at crevasse tips in dense fields of crevasses. As ice is advected into a stress field that favors crevasse formation, the depth to which a newly-formed crevasse penetrates depends on the instantaneous stress state as well as the micro- and macro-scale damage that the parcel of ice has inherited throughout its history (Bassis and Jacobs, 2013). If a crevasse penetrates deeper than its surrounding crevasses, then it will reduce the stresses on its neighbors, which will penetrate shallower than inherently

335   assumed by the Nye formulation (van der Veen, 1998). Propagation is favored at the deepest crevasses as they advect through extensional flow regimes, as supported by the observed along-flow increase in maximum crevasse depths observed at over half of our glaciers. Although the Nye formulation may accurately model the depths of closely-spaced crevasses in an idealized setting, its assumptions that (1) crevasse depth is a function of the local stress state and (2) stress concentration at crevasse tips can be ignored in closely-spaced crevasse fields, are invalid for the complicated stress histories at fast-flowing outlet glaciers.

340

The inability of the Nye formulation to simulate the complex patterns in observed crevasse depths is problematic for a number of reasons. We focus on implications for numerical ice flow modeling here since the over-prediction of crevasse depths may result in undue emphasis on the role of surface crevassing as a control on recent and future changes in terminus position of fast-flowing marine-terminating glaciers. However, our analysis of observed and modeled crevasse depths also suggests that

345   advection of crevasses, and their associated mechanical and thermodynamic softening of ice, may exert an important control on the glacier stress balance. Confident projections of dynamic mass loss therefore require additional investigations on crevassing, including the impacts of effects of spatio-temporal variations in crevassing on hydrologic routing, flow enhancement via damage and cryohydrologic warming, and iceberg calving. We anticipate that these findings will spur novel efforts to model crevasse formation that pursue approaches different than that of the Nye formulation.

350

References

Andreas, E.: Parameterizing scalar transfer over snow and Ice: A review, J. Hydrometeor., 3, 417–432, 2002.

355   Bassis, J. N. and Jacobs, S.: Diverse calving patterns linked to glacier geometry, Nat. Geosci., 6, 833-836, doi:10.1038/ngeo1887, 2013.

Benn, D. I., Warren, C. R. and Mottram, R. H.: Calving processes and the dynamics of calving glaciers, Earth-Sci. Rev., 82, 143-179, 2007a.

Benn, D. I., Hulton, N. R. J. and Mottram, R. H.: 'Calving laws', 'sliding laws' and the stability of tidewater glaciers, A.
360   Glaciol., 46, 123-130, 2007b.

Bjork, A. A., Kruse, L. M. and Michaelsen, P. B.: Brief Communication: Getting Greenland's glaciers right – a new dataset of all official Greenlandic glacier names, The Cryo., 9, 2215-2218, doi:10.5194/tc-9-2215-2015, 2015.

Carr, J. R., Stokes, C. R. and Vieli, A.: Threefold increase in marine-terminating outlet glacier retreat rates across the Atlantic Arctic: 1992–2010, A. Glaciol., 58(74), 72–91, doi:10.1017/aog.2017.3, 2017.

365   Cathles, M., Abbot, D., Bassis, J. and MacAyeal, D.: Modeling surface-roughness/solar-ablation feedback: Application to small-scale surface channels and crevasses of the Greenland ice sheet, A. Glaciol., 52, 99–108, 2011.

Colgan, W., Rajaram, H., Abdalati, W., McCutchan, C., Mottram, R., Moussavi, M. S. and Grigsby, S.: Glacier crevasses: Observations, models, and mass balance implications, Rev.Geophys., 54, doi:10.1002/2015RG000504, 2016.

Colgan, W., Steffen, K., McLamb, W., Abdalati, W., Rajaram, H., Motyka, R., Phillips, T. and Anderson, R.: An increase in
370   crevasse extent, West Greenland: Hydrologic implications, Geophy. Res. Lett., 38, L18502, doi:10.1029/2011GL048491, 2011.

Cook, S., Zwinger, T., Rutt, I. C., O'Neel, S. and Murray, T.: Testing the effect of water in crevasses on a physically based calving model, A. Glaciol., 53, 90–96, 2012.

Cook, S., Rutt, I. C., Murray, T., Luckman, A., Zwinger, T., Selmes, N., Goldsack, A. and James, T. D.: Modelling
375   environmental influences on calving at Helheim Glacier in eastern Greenland, The Cryo., 8, 827-841, doi: 10.5194/tc-8-827-2014, 2014.

Hock, R.: Glacier melt: A review of processes and their modelling, Prog. Phys. Geog., 29, 362–391, 2005.

Howat, I.M. and Eddy, A.: Multi-decadal retreat of Greenland's marine-terminating glaciers, J. Glaciol., 57(203), 389-396, 2011.

380   Moon, T.K. and Joughin, I.: Retreat and advance of Greenland tidewater glaciers from 1992 to 2007, J. Geophys. Res., 113, F02022, doi:10.1029/2007JF000927, 2008.

Mottram R. H. and Benn, D. I.: Testing crevasse-depth models: a field study at Breiðamerkurjökull, Iceland, J. Glaciol., 55(192), 746-752, 2009.

Nick, F. M., Vieli, A., Anderson, M. L., Joughin, I., Payne, A., Edwards, T. L., Pattyn, F. and van de Wal, R. S. W.: Future
385   sea-level rise from Greenland's main outlet glaciers in a warming climate, Nature, 497, 235–238, doi:10.1038/nature12068, 2013.

The Cryosphere
Discussions

Noh, M. -J. and Howat, I. M.: Automated stereo-photogrammetric DEM generation at high latitudes: Surface Extraction with TIN-based Search-space Minimization (SETSM) validation and demonstration over glaciated regions, GIS. Rem. Sens., doi:10.1080/15481603.2015.1008621, 2015.

390   Nye, J.F.: The distribution of stress and velocity in glaciers and ice sheets, Proc. Roy. Soc. London. Series A, 239, 113–133, 1957.

Otero, J., Navarro, F. J., Lapazaran, J. L., Welty, E., Puczko, D. and Finkelnburg, R.: Modeling the controls on the front position of a tidewater glacier in Svalbard, Front. Earth Sci., 5, 29, doi:10.3389/feart.2017.00029, 2017.

Pfeffer, W. and Bretherton, C.: The effect of crevasses on the solar heating of a glacier surface, Int. Assoc. Hydro. Sci. Pub.s: The Physical Basis of Ice Sheet Modelling 170, 191–205, 1987.

Pollard, D., DeConto, R. M. and Alley, R. B.: Potential Antarctic Ice Sheet retreat driven by hydrofracturing and ice cliff failure, Earth Planet. Sci. Lett., 412, 112-121, doi: 10.1016/j.epsl.2014.12.035, 2015.

Poinar, K., Joughin, I., Lilien, D., Brucker, L., Kehrl, L. and Nowicki, S.: Drainage of Southeast Greenland firn aquifer water through crevasses to the bed, Front. Earth Sci., 5, 5, doi:10.3389/feart.2017.00005, 2017.

400   Reese, R., Gudmundsson, G. H., Levermann, A. and Winkelmann, R.: The far reach of ice-shelf thinning in Antarctica, Nature Clim. Change, 8, 53-57, doi: 10.1038/s41558-017-0020-x, 2018.

Rott, H., Skvarca, P. and Nagler, T.: Rapid collapse of northern Larsen Ice Shelf, Ant. Sci., 271, 788–792, 1996.

Scambos, T. A., Hulbe, C., Fahnestock, M. and Bohlander, J.: The link between climate warming and break-up of ice shelves in the Antarctic Peninsula, J. Glaciol., 46, 516–530, doi:10.3189/172756500781833043, 2000.

405   Scambos, T. A., Fricker, H. A., Liu, C. -C., Bohlander, J., Fastook, J., Sargent, A., Massom, R. and Wu, A.-M.: Ice shelf disintegration by plate bending and hydro-fracture: Satellite observations and model results of the 2008 Wilkins ice shelf break- ups, Earth Planet. Sci. Lett., 280, 51–60, doi:10.1016/j.epsl.2008.12.027, 2009.

Stevens, L. A., Behn, M. D., McGuire, J. J., Das, S. B., Joughin, I., Herring, T., Shean, D. E. and King, M. A.: Greenland supraglacial lake drainages triggered by hydrologically induced basal slip, Nature, 522, 73-76, 2015.

410   Trantow, T. and Herzfeld, U.C.: Crevasses as Indicators of Surge Dynamics in the Bering Bagley Glacier System, Alaska: Numerical Experiments and Comparison to Image Data Analysis, J. Geophys. Res.: Earth Surf., 123(8), 1615-1637, doi:10.1029/2017JF004341, 2018.

Van der Veen, C. J.: Fracture mechanics approach to penetration of surface crevasses on glaciers, Cold Reg. Sci. Technol., 27(1), 31–47, 1998.

415   Vieli, A. and Nick, F. M.: Understanding and modeling rapid dynamic changes of tidewater outlet glaciers: Issues and implications, Surv. Geophys., 32, 437–458, doi:10.1007/s10712-011-9132-4, 2011.
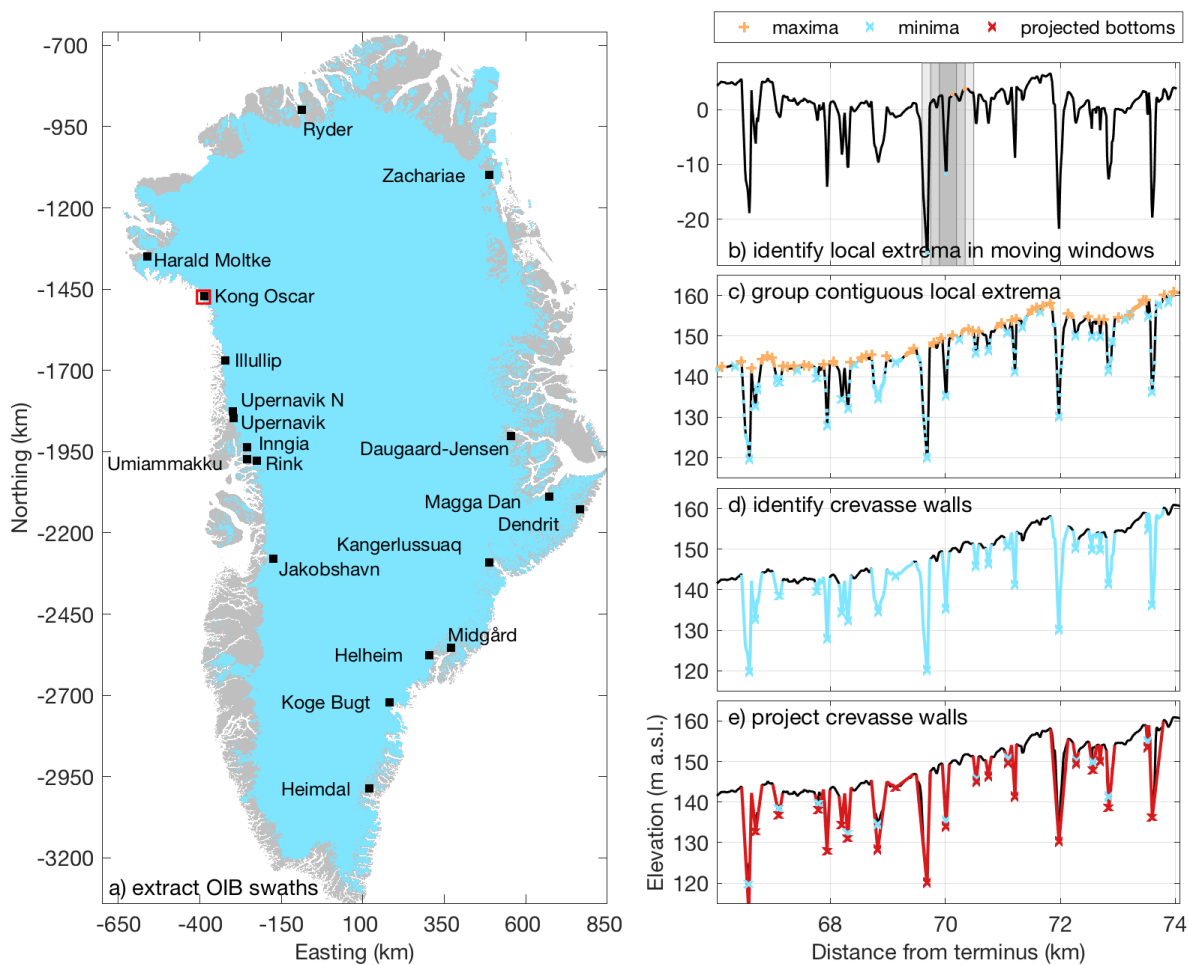
Figure 1: Map of glacier locations and example of the crevasse depth estimation approach applied to the elevation data for each glacier. a) Operation IceBridge transects (black squares) overlain on the Greenland Ice Mapping Project ice mask (light blue) and land mask (gray). Glacier names are from Bjork et al. (2015). The red box highlights the location of the profile in panels b-e. b) Moving window approach to find local extrema. The nested search windows (gray shading) and local extrema (colored points) overlain on the de-trended portion of the profile. Local extrema were filtered to c) isolate crevasse bottoms (blue x's) and top edges (orange +'s), d) locate steeply-sloped crevasse walls (blue lines), and e) project wall slopes to depth.
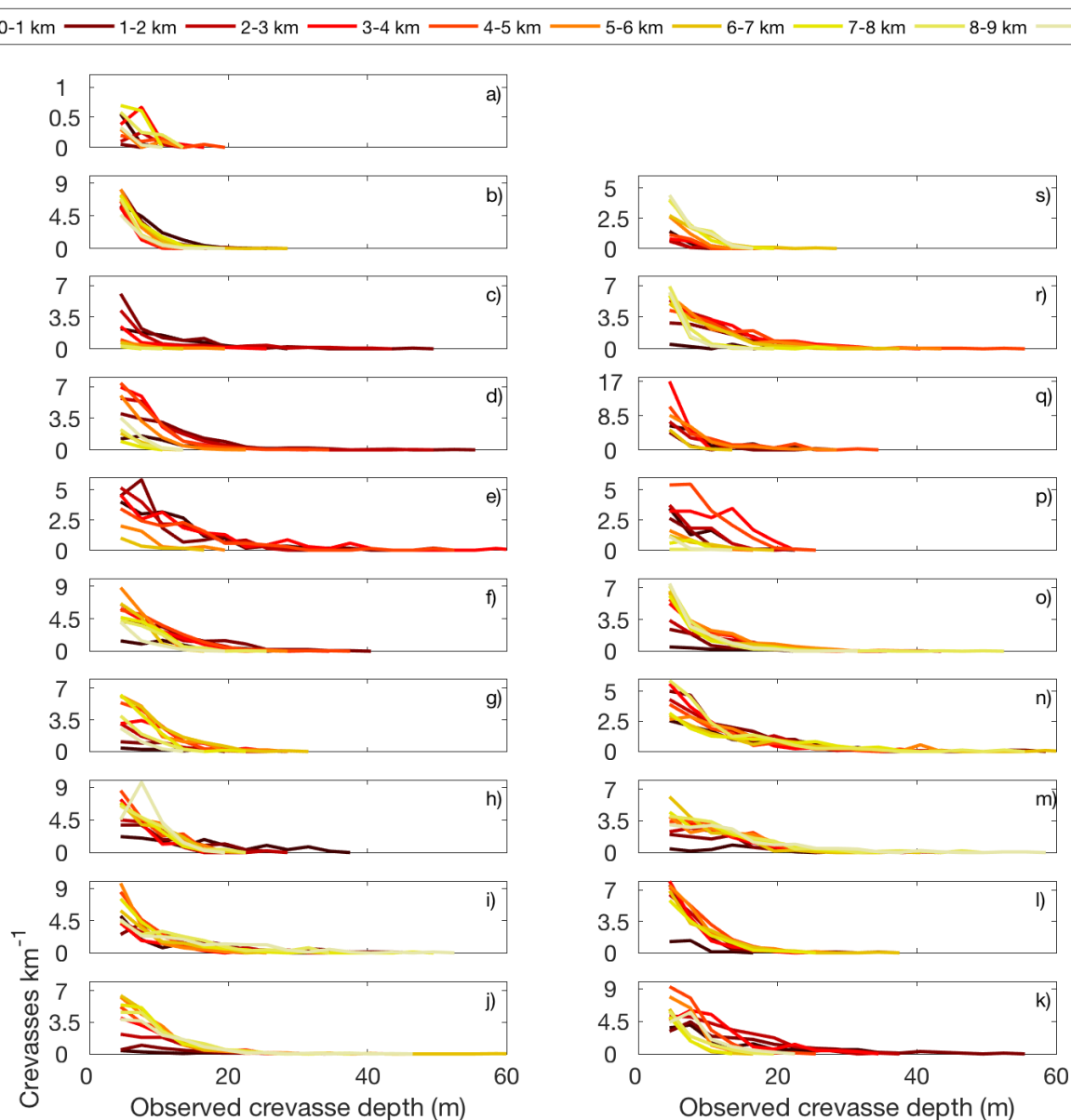
Figure 2: Observed crevasse depth distributions for 1km-wide bins over the first 10km of each glacier. The distance from the terminus of each bin is distinguished by line color. Differences in area under the curves reflect variations in observed crevasse concentration between bins. Panels are geographically arranged so that western glaciers are on the left and eastern glaciers are on the right. Common names (Greenlandic names) are a) Ryder Gletsjer, b) Harald Moltke Bræ (Ullip Sermia), c) Kong Oscar Gletsjer (Nuussuup Sermia), d) Illiup Sermia, e) Upernavik North Isstrøm, f) Upernavik Isstrøm (Sermeq), g) Inngia Isbræ (Salliarutsip Sermia), h) Umiammakku Sermiat, i) Rink Isbræ (Kangilliup Sermia), j) Jakobshavn Isbræ (Sermeq Kujalleq), k) Heimdal Gletsjer, l) Koge Bugt Gletsjer, m) Helheim Gletsjer, n) Midgård Gletsjer, o) Kangerlussuaq Gletsjer, p) Dendrit Gletsjer, q) Magga Dan Gletsjer, r) Daugaard-Jensen Gletsjer, s) Zachariae Isstrøm.

15
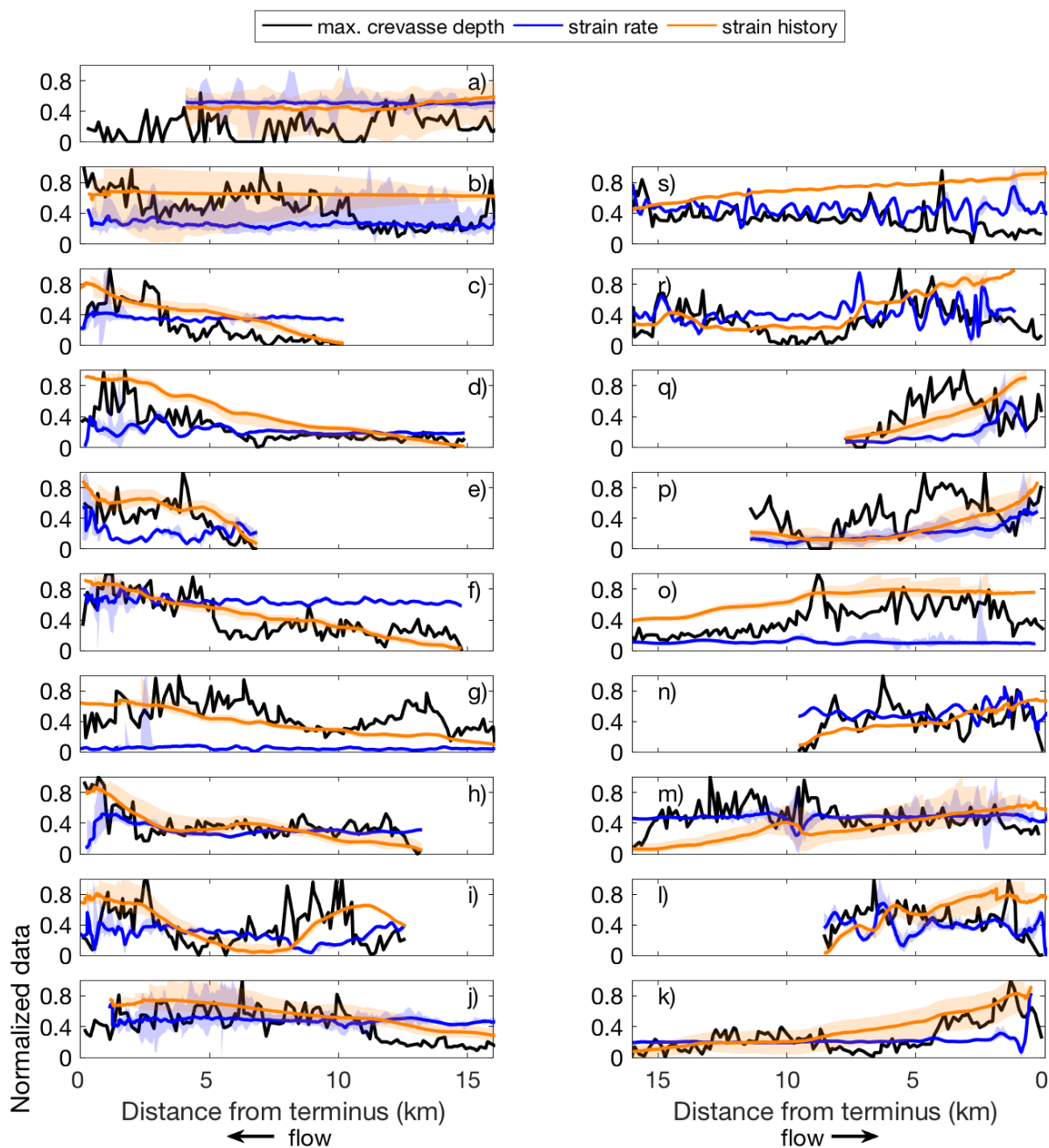
Figure 3: Normalized profiles of maximum crevasse depth, local strain rate, and strain history. In each panel, the maximum crevasse depth in 150 m-wide bins is in black, the local strain rate is in blue, and the strain history is in orange. The median strain rate and strain history are shown as lines with shading indicating their temporal ranges. As in Fig. 2, the panels are geographically arranged.
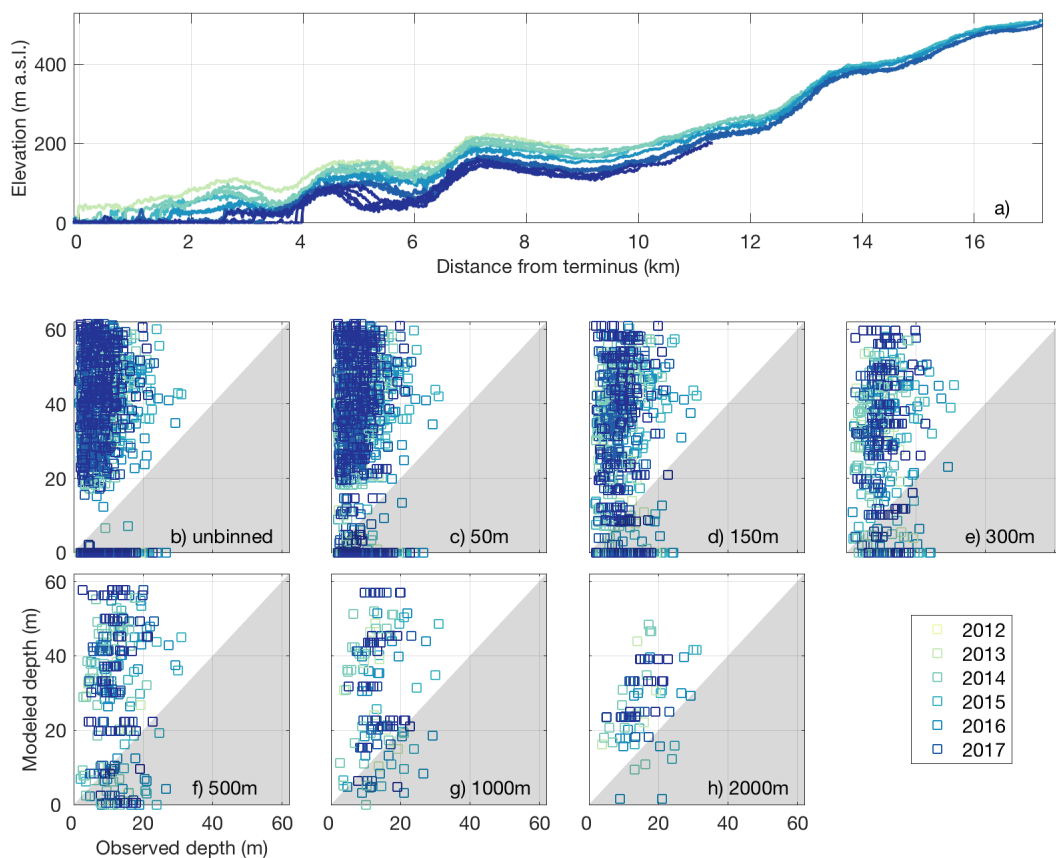
Figure 4: Inngia Isbræ (Greenlandic Name: Salliarutsip Sermia) crevasse depth data. The legend indicates the observation year for all panels. a) Elevation profile time series extracted along the OIB swath. b-h) Scatterplots of observed crevasse depths plotted against modeled crevasse depths. Points that fall in the white (gray) region represent model over-estimates (under-estimates) of observed depths. All observations are shown in b whereas the maximum observed and median modeled depths within along-flow bins are shown in c-h. The bin sizes in c-h (50-2000 m) reflect the range of spatial resolutions for numerical ice flow models.
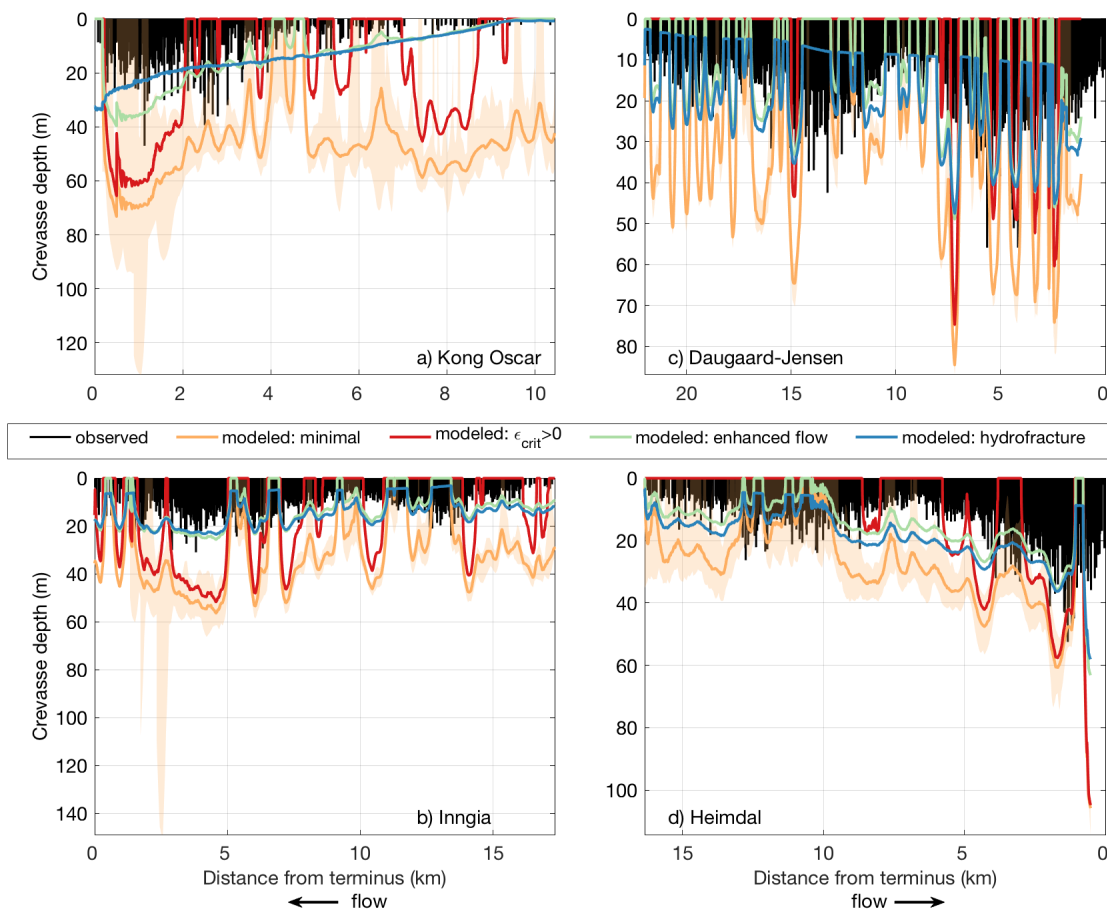
Figure 5: Profiles of all observed crevasse depths (black lines) and modeled crevasse depths (colored lines) computed from the median velocity profile for a) Kong Oscar Gletsjer, b) Inngia Isbræ, c) Daugaard-Jensen Gletsjer, and d) Heimdal Gletsjer. Orange colors show the median (line) and temporal range (shading) in modeled crevasse depths using the minimal Nye formation (i.e., no critical strain rate, uniform viscosity, no water). The red, green, and blue lines show the modeled crevasse depths with observation-based critical strain rates, flow enhancement, and flow enhancement with impounded water, respectively.

Glacier Name	Latitude (°N)	Longitude (°E)	Maximum Observed Depth (m)	Median Observed Depth (m)	Concentration (crevasses/km)	Maximum Modeled Depth (m)	Median Modeled Depth (m)	Deformation Enhancement (unitless)	Maximum Water Depth (m)
Ryder	81.7802	-50.4556	10.9	4.8	1.0	29.4	15.2	0.64	6.1
Harald Moltke	76.5718	-67.5659	21.1	3.3	15.2	34.8	22.2	0.63	10.2
Kong Oscar	76.0267	-59.7052	47.0	5.0	9.6	69.7	46.6	0.79	*32.7*
Illullip	74.4026	-55.9341	46.6	6.3	16.9	90.8	62.9	0.77	*25.0*
Upernavik North	72.9511	-54.1183	59.9	8.6	17.8	118.5	52.2	0.70	*30.7*
Upernavik	72.8461	-54.1578	36.3	7.6	19.6	69.6	41.4	0.58	*10.8*
Inngia	72.1022	-52.5047	29.3	6.2	17.2	56.4	33.8	0.64	6.4
Umiammakku	71.7685	-52.3880	35.3	6.9	15.2	64.7	39.1	0.55	9.4
Rink	71.7381	-51.6096	31.6	5.9	21.9	72.3	49.7	0.62	13.1
Jakobshavn	69.1166	-49.4560	58.6	7.3	17.9	72.3	61.9	0.67	28.1
Heimdal	62.8969	-42.6730	24.0	5.4	18.5	33.8	28.2	0.58	12.7
Koge Bugt	65.2097	-41.2156	35.1	5.9	17.3	106.3	58.2	0.76	8.7
Helheim	66.3941	-38.3800	64.9	10.2	15.0	51.5	37.1	0.38	5.8
Midgård	66.5119	-36.7300	55.4	9.3	19.0	108.2	56.8	0.54	14.0
Kangerlussuaq	68.5864	-32.8397	50.0	4.5	17.8	80.8	45.9	0.70	*27.9*
Dendrit	69.3449	-25.1687	23.9	6.5	11.4	52.8	35.2	0.62	*7.3*
Magga Dan	69.9375	-27.1410	33.1	5.3	18.6	76.2	49.4	0.72	4.0
Daugaard-Jensen	71.8797	-28.6788	55.9	7.2	16.2	84.5	38.1	0.53	12.0
Zachariæ	78.9161	-21.0828	19.1	5.3	6.8	84.5	47.3	0.77	3.2

Table 1: Observed and modeled crevasse characteristics. The name, location, maximum and median observed crevasse depths, median concentration of crevasses within 5km of the terminus, maximum and median modeled crevasse depth within 5km of the terminus, median deformation enhancement factor, and maximum water depth estimate for each study site.